Dynamical reconstruction of the upper-ocean state in the Central Arctic during the winter period of the MOSAiC Expedition

Ivan Kuznetsov[a], Benjamin Rabe[a], Alexey Androsov[a], Ying-Chih Fang[b], Mario Hoppmann[a],
Alejandra Quintanilla-Zurita[a], Sven Harig[a], Sandra Tippenhauer[a], Kirstin Schulz[c], Volker Mohrholz[d],
Ilker Fer[e], Vera Fofonova[a], and Markus Janout[a]

[a]Alfred-Wegener-Institut Helmholtz-Zentrum für Polar- und Meeresforschung, Bremerhaven, Germany
[b]National Sun Yat-sen University University, 80424 Kaohsiung, Taiwan
[c]Oden Institute for Computational Engineering and Sciences, The University of Texas at Austin, Austin, TX, United States
[d]Leibniz-Institute for Baltic Sea Research Warnemünde, Germany
[e]Geophysical Institute, University of Bergen and Bjerknes Center for Climate Research, Bergen, Norway

Correspondence: Ivan Kuznetsov (ivan.kuznetsov@awi.de)

Abstract. The Arctic Ocean is a region important for global and regional climate. Although generally quiescent compared to mid-latitudes, the upper Arctic ocean hosts mesoscale and smaller scale processes. These processes can have a profound impact on vertical ocean fluxes, stratification, and feedback with the sea ice and atmosphere. Sparse and non-synoptic in-situ observations of the polar oceans are limited by the distribution of manual observing platforms and autonomous instrumen-
5 tation. Analyzing observational data to assess tracer field gradients and upper ocean dynamics becomes highly challenging when measurement platforms drift with the ice pack due to continuous changes in drift speed direction. This work presents a dynamical reconstruction of the ocean state, based on observations of the Multidisciplinary Observatory for the Study of Arctic Climate (MOSAiC) experiment. Overall, the model can reproduce the lateral and vertical structure of the temperature, salinity, and density fields, which allows for projecting dynamically consistent features of these fields onto a regular grid. We identify
10 two separate depth ranges of enhanced eddy kinetic energy, which are located around two maxima in buoyancy frequency: the depth of the upper halocline and the depth of the warm (modified) Atlantic Water. Simulations reveals a notable decrease in surface layer salinity and density towards the north, accompanied by high variability in the mixed layer depth in the south-north direction. And no significant horizontal gradients in salinity and density fields but an increase in mixed layer depth from west to east 0.084 m/km gradient with 0.6 m/km standard deviation, indicating opposite characteristics compared to the south-north
15 direction. The model resolves several stationary eddies in the warm Atlantic Water and provides insights into the associated dynamics. The obtained three-dimensional fields of temperature and salinity can be used for further analysis of the thermo-haline structure and related dynamics associated with submesoscale processes in the Central Arctic. Dynamic characteristics and eddy fields can be used for further analysis and comparison with state-of-the-art climate and Earth System Models. The developed nudging method can be used to utilize future observational data obtained from a diverse set of instruments.

1 Introduction

Mesoscale eddies and submesoscale eddies whose scales respectively larger or smaller than the local baroclinic deformation radius have been observed in many parts of the world's oceans, including the Arctic. Eddy-driven fluxes play a significant role in Arctic Ocean dynamics, such as the ventilation of the halocline, and the transport of organic and inorganic matter, e.g. nutrients and carbon, heat and salt (Dmitrenko et al., 2008; Meneghello et al., 2021; Marcinko et al., 2015; Pnyushkov et al., 2018; Mahadevan, 2016; Mahadevan et al., 2010; Gula et al., 2022; Nishino et al., 2018; Watanabe, 2011). The majority of studies on under-ice eddy dynamics in the Arctic are focused on the ice edge and shelf break zone, where the eddy activity is maximal, but little is known about eddies in the ice-covered central Arctic Ocean.

Analyzing Ice-Tethered Profiler and mooring data in the Canada Basin Zhao et al. (2016) have shown that eddy activity is subject to high interannual variability. Pnyushkov et al. (2018) found, based on mooring observations, that eddies in the area of the boundary current in the eastern Eurasian Basin appear about once per month and have a significant role in the vertical transfer of heat within the Arctic Ocean interior. Detailed three-dimensional analyses of an Arctic eddy and what the associated ramifications, prevailing on the order of months in the Chukchi Sea, were conducted by Scott et al. (2019), based on the data from a rapid shipboard survey. By studying submesoscale flows in the ice-covered Arctic, Mensa and Timmermans (2017) have shown that local eddies are responsible for significant vertical heat fluxes, and stimulate mixed layer (ML) restratification. Based on observations and eddy-resolving model results, von Appen et al. (2022) argued that eddy kinetic energy (EKE), i.e. the intensity of the mesoscale dynamics, is 100 to 1000 times smaller in the basin compared to the shelf break region. Moreover, it was found that EKE is stronger in areas with low sea ice concentrations. Applying an idealized model in the marginal ice zone, Manucharyan and Thompson (2017) found that submesoscale flows could significantly increase the horizontal eddy diffusivity of sea ice mass, heat, and vertical velocities. Using the results of high-resolution modeling and observational data, Meneghello et al. (2021) show that surface mesoscale activity is extremely low during the winter period, due to fast energy dissipation by friction between eddies and sea ice. The authors show that mesoscale eddies found in the subsurface can be explained by the baroclinic stratification and potential vorticity gradients commonly present in the Arctic interior.

Despite the intensification of mesoscale dynamics at the basin boundaries, von Appen et al. (2022) note that in the central Eurasian Basin, EKE is significant in both the halocline and the Atlantic Water layer, according to the high-resolution simulation. Meneghello et al. (2021) also note the presence of EKE maxima in two layers of maximum density gradients in the Canada basin. Androsov et al. (2005) and Rubino et al. (2007) investigated the non-stationarity of dynamics and evolution of mesoscale chimneys in the Greenland Sea. The use of in situ observations together with 3D non-hydrostatic modeling and the analytical solution allowed the authors to investigate inertial pulsations, shape, and velocity structure of eddy, and their significant effect on open-ocean deep-penetrating convection. An analysis of the dynamics of baroclinic vortices in stratified fluids, and the associated mass and heat transports, based on theoretical developments and numerical methods is given in Sokolovskiy and Verron (2013).

Furthermore, eddy dynamics impact biochemical processes in the Arctic Ocean. Llinás et al. (2009) illustrate the possible mechanism of zooplankton transport from the Chukchi Shelf into the interior Canada Basin by eddies. O'Brien et al. (2013)

found a significant role of eddies on the particle flux, and Oziel et al. (2022) demonstrate in a modelling study that lateral submesoscale eddy transport is one of the dominating process controlling the nitrate supply in the central Arctic Ocean. Omand et al. (2015) show that small-scale vorticity could be responsible for high concentrations of particulate organic carbon in deeper layers. According to their calculations, submesoscale, eddy-driven fluxes can contribute as much as half of the total springtime export of particulate organic carbon from the upper ocean to deeper layers in the subpolar region. Using coupled physical and ecosystem models, Lovecchio et al. (2022) demonstrate the difference in trapping efficiencies of cyclonic and anticyclonic long-living mesoscale eddies, impacting the biogeochemical processes within the ocean.

Despite ongoing efforts to develop and improve climate models, the accurate representation of submesoscale dynamics remains a challenge. Androsov et al. (2020) compared ocean models with various horizontal resolutions to observed ocean bottom pressure, and found only a modest correlation between the models and observations. They conclude that high resolution is necessary in areas with high mesoscale eddy activity. According to Zhao et al. (2014), the radii of observed halocline mesoscale eddies in the Arctic Ocean are on the order of a few kilometers. The first baroclinic Rossby deformation radius here varies between 1 to 15 km (Nurser and Bacon, 2014). The necessity to resolve such small scales makes it challenging to explicitly model submesoscale features in global climate models due to the lack of horizontal resolution. Recent developments in ocean climate models, software, and hardware give a possibility for simulations with a very high horizontal resolution, for example Wang et al. (2020); Maslowski et al. (2008); Regan et al. (2020); Lyu et al. (2022); Hordoir et al. (2022).

Most studies on eddy dynamics in the Arctic have focused on the marginal ice zone or coastal currents, the main limitation of submesoscale research in the central Arctic being observational data. Unfortunately, standard methods for observing eddies, such as satellite remote sensing or glider and transect campaigns, have so far been challenging in near-perennially ice-covered seas. To fill the gap in research of mesoscale and submesoscale dynamics in the central Arctic Ocean, during the Multidisciplinary Observatory for the Study of Arctic Climate (MOSAiC, e.g. Rabe et al., 2022) expedition, autonomous ice-tethered systems ("buoys") were distributed radially around the Central Observatory (CO). The CO included a series of autonomous buoys, the R/V *Polarstern* and the so-called Ocean City (OC), about 300 m away from the ship. This setup enabled us to obtain regular, non-autonomous measurements. The large number of extremely diverse observations during the MOSAiC expedition, from point measurements to profiles, differ significantly both in temporal frequency, from irregular weekly measurements to measurements every 2 minutes, and in spatial resolution, from tens of kilometers to tens of meters. Moreover, the looping of the DN drift trajectory and the intersection of the trajectories of different buoys add complexity to the observed data. Nevertheless, using relatively simple data analysis methods, several mesoscale eddies were identified in the Amundsen Basin (Hoppmann et al., 2022; Fang et al., 2023 (submitted; Quintanilla-Zurita and et al., (in prep.). However, these methods have limitations in showing the overall 3D picture, as the buoy measurements can be complex to analyze spatially, due to the above mentioned complex drift trajectories. As a result, estimating lateral gradients of tracers or velocity shear are challenging, and the question remains how to best analyze such scattered data and dynamics, and their role in vertical transport. One possible method are interpolation techniques. However, the lateral scales of phenomena on interpolated maps can be limited by distances between the observing buoy systems or parameters of the interpolation algorithm, rather than physical processes. Reconstructing temperature, salinity, and density fields with a model by data assimilation allows for the estimation of dynamically consistent lateral

features of these fields on a regular grid. Assimilating high-frequency variability data, however, presents its own significant
90 challenges: First, the assimilation time (usually once every 10 days or even daily averaging in extreme cases) significantly
increases computation time. Second, the assimilation process involves averaging over a significant data radius, resulting in a
smoothing effect on the assimilated data (Androsov et al., 2018). The nature of the data has to be considered when employ-
ing advanced methods such as the four-dimensional variational method (Courtier et al., 1994; Mogensen et al., 2009) or the
Parallel Data Assimilation Framework (Nerger et al., 2020). Unfortunately, the high-frequency variability and the scales of the
95 observations inherent in the MOSAiC data make it impractical to apply these methods to eddy analysis. Alternatively, nudging
has several advantages for ocean data assimilation, including its ease of implementation in complex numerical models, its low
computational demands, and the smoothness of the solution over time (Ruggiero et al., 2015).

The aim of our study is to extend current knowledge of submesoscale dynamics in the central Arctic by using the 3D
regional model FESOM-C with very high vertical and horizontal resolution. We utilize observed temperature and salinity
100 data from the MOSAiC DN buoys as part of the forcing for the numerical model. Our objective was to design a tool that
could reconstruct water properties based on MOSAiC DN observational data and to reconstruct temperature and salinity fields
with submesoscale variability using the high-resolution modeled dynamics. Additionally, we aim to estimate the properties of
submesoscale dynamics during the MOSAiC expedition.

This paper is organized as follows. Section 2 presents the numerical model, observations, new nudging methodology, and
105 experimental design. In section 3, we present the results of simulations and model validation. The analysis of (sub)mesoscale
dynamics and distribution of eddy kinetic energy from the reconstructed dynamical fields are discussed in Section 4. In section
4.4 we summarize the results.

2 Methods

2.1 FESOM-C model

110 The FESOM-C model used in this work (Danilov and Androsov, 2015; Androsov et al., 2019) is a coastal branch of the global
Finite volumE sea ice–Ocean Model (FESOM2) (Danilov et al., 2017). In addition to the partially common interface of the
models, FESOM-C has specific features that are important for our work. The model was originally developed for applications
with a high horizontal resolution as fine as several meters (Neder et al., 2022; Kuznetsov et al., 2020; Fofonova et al., 2019).
This model uses the discretization of cells and vertices of a finite volume, which allows the use of unstructured computational
115 grids. We use this function to move the boundary of the computational domain away from the region of interest, the "core"
of the model grid, without creating a system of nested grids. At the same time, the horizontal resolution outside the core is
quite coarse, which allows us to reduce the influence of the boundary on our solution inside the core. The most important
distinguishing feature from the global FESOM2 model is the possibility of using hybrid grids consisting of triangles and
squares. The effectiveness of this approach to enhance stability and using larger time steps is shown by Danilov and Androsov
120 (2015) and Androsov et al. (2019).

The parallel Algebraic Recursive Multilevel Solver (pARMS, (Li et al.)) used in FESOM2 was used to calculate the sea level using a semi-implicit method. Since we study the processes in the deep-water region, where the effect of bottom friction is minimal and the barotropic mode does not play a key role, we modified the scheme to a semi-implicit calculation of the sea level, omitting the solution of the block of average equations.

125 The thermodynamics of the sea ice model component has not been used in the current work. Alteration of the ocean surface temperature and salinity due to ice formation and melting has been forced by data nudging. The effect of sea ice presence on the dynamics of the ocean surface layer has been parameterized by the friction between ice and ocean. The effect of ice drift has been accounted for in the turbulence closure and is described in the following section.

In contrast to previous publications, we have implemented parallel calculations based on the Message Passing Interface
130 (MPI). For the dynamic part of the model, the MPI scheme is similar to that of FESOM2 but applied to hybrid grids. The organization of parallel output and input for boundary conditions at open surface boundaries, in contrast to the global model, were written using the PnetCDF library (Li et al., 2003). This made it possible to take advantage of the flexibility of the previous openMP FESOM-C I/O version.

2.2 Turbulence closure

135 The turbulence closure equation based on the Prandtl-Kolmogorov hypothesis described in Androsov et al. (2019) is used to calculate turbulent vertical flows. Compared to the original version of the FESOM-C model, the modification of this equation concerned only the parametrization of the turbulence scale l. The need for this change is associated primarily with the parametrization of the ice-water layer and a more dynamic description of the moving ML. At the preliminary stage, an average upper bound ice-drift velocity is estimated at 0.7 m/s, which is used as an upper boundary condition for the dynamic wind speed in the turbulent energy budget equation. In the second stage, the thickness of the ML h_{ml} is estimated as the depth with
140 a practical salinity increase of 0.5 from the surface value, but minimum 20 meters. Then, the scale of turbulence in the upper ML is determined by

$$l = \frac{\kappa}{h_{ml}} \cdot Z_H \cdot Z_\zeta, \tag{1}$$

where $Z_H = z + h_{ml}$, $Z_\zeta = z + z_\zeta$, $\kappa \sim 0.4$ is the von Kármán constant and z_ζ is the roughness parameter for the ice-water
145 layer. Underneath the surface ML h_{ml}, the scale of turbulence is given by:

$$l = \frac{\kappa}{H - h_{ml}} \cdot Z_H \cdot Z_{ml} \cdot C, \tag{2}$$

where $H = h + \zeta$ is the full water depth, $Z_{ml} = -z + (H - h_{ml}) + z_b$, z_b is the roughness parameter for the bottom and the constant $C \sim 0.01$ is set to reduce the scale of turbulence underneath the ML. This approach to determine the scale of turbulence ensures the smoothness and minimization of turbulent exchange at the boundary of the ML and the water column underneath
150 the ML.

2.3 Model domain

The model domain is a parallelepiped in Cartesian coordinates with a solid boundary. Since the FESOM-C model allows computing on mixed unstructured meshes, we can adjust the spatial resolution without using nested grids. For the final computations, two spatial configurations of the model are used. The general conditions for these configurations were that, near the horizontal boundaries of the domain, the spatial resolution was relatively coarse, about 5 km. Such a coarse resolution at the boundaries serves two purposes: First, absorption due to the more strong dissipation of the uncertainty of the boundary information and its leveling to calculations in the core of the model is the most important in our application. Second, there are significant savings in computational resources. The first configuration of the model has a resolution of up to 1 km in the area of interest and contains 96000 nodes. This setup is mainly used at the initial modeling stage to form the initial conditions for a spatially detailed configuration of the study domain. The second configuration has a resolution of up to 250 m at the model's core and contains about 1.3 million nodes (see Figure 1). This setup is used for the final computations and data analysis. The vertical structure is the same for both configurations and contains 240 vertical σ-layers. At the same time, the upper layer up to 150 m has an effective resolution of up to one meter, which makes it possible to significantly improve the representation of the vertical aspects of the submesoscale dynamics of surface ML compared to global models. The model domain is about 660 by 525 kilometers and limited geographically to between 90° East and 140° East longitude as well as 83° North and 87.7° North latitude.

2.4 Observational data

Here we use an observational data set obtained as part of the physical oceanography work program during the field phase of the Multidisciplinary Observatory for the Study of Arctic Climate (MOSAiC) in 2019/20 (Shupe et al., 2020). A description of the physical oceanography part of the experiment with a general description of the instruments and methodology is presented in Rabe et al. (2022). Temperature and salinity observations used in this work were obtained by various instruments: Most of the data was measured by autonomous ice-tethered systems ("buoys") within the DN originally deployed by the icebreaker *Akademik Fedorov* (Krumpen and Sokolov, 2020) radially around the icebreaker *Polarstern* tethered to the sea ice at the Central Observatory. Eight buoys termed "Salinity-Ice-Tether" (SIT) measured temperature, conductivity, and pressure, with derived salinity and depth, at five depths of 10, 20, 50, 75, and 100 meters with a sampling interval of 2 to 10 minutes, with a distance between subsequent data points as small as 80 meters. The sensors used on these buoys have an initial accuracy of ±0.003 mS cm^{-1} for conductivity, ±0.002 °C for temperature, and ±0.1% of the full range for pressure. The sensor stability rating is 0.003 mS cm^{-1} and 0.0002 per month for conductivity and temperature, respectively, with a yearly rating of 0.05% of the full scale for pressure. The detailed description of the instruments and the data obtained are given by Hoppmann et al. (2022). We further, used data from three Ice-tethered profilers (ITP; Toole and Krishfield, 2016). The time between subsequent profiles varied from several hours to days, depending on the specific system. The maximum depth reached by these profilers was about 700 m. Thus, the measurements with profilers cover depths in the warm waters of Atlantic origin (referred to as "warm Atlantic Water") and beyond. A total of 1114 profiles was used for nudging. The nudging process included additional profiles
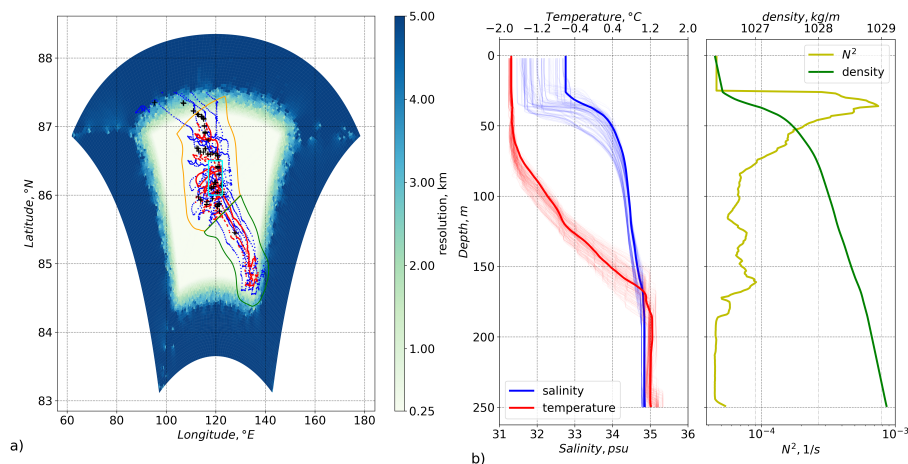
Figure 1. a) - Model domain resolution with the position of the observational data used in this study, covering a time period of ≈2.5 months. The positions of the observational data used for nudging are separated by instrument type: blue - 5 SIT buoys, with CTDs at 10,20,50,75,100 meters depth (Hoppmann et al., 2022). red – PS- and OC-CTD casts (Tippenhauer et al., 2023a, b), and ITP profiles (Toole and Krishfield, 2016). Black crosses - position of MSS profiles used for validation Schulz et al. (2022). The green polygon indicates an area with mainly straight drift trajectories, whereas the orange polygon indicates an area with often overlapping buoy trajectories. The cyan rectangle shows the area of Figure 9. b) - bold lines temperature, salinity, density, and N2 profiles used as initial conditions in the model; thin lines - profiles of the independent MSS data used for the model validation (see Section 3.1).

from CTD/rosette casts at the Central Observatory, both from *Polarstern* (PS-CTD; 25 profiles with depths up to 4450 meters)
185 (Tippenhauer et al. (2023a)) and from a location a few hundred meters away from the ship, at the so-called "Ocean City" (OC-CTD; 44 profiles up to 500 meters) (Tippenhauer et al. (2023b)). ITP profiles with unstable stratification or a vertical range of less than 10 m were excluded from the analysis. Data from the profiles were averaged with a standard pressure interval of 1 dbar (a depth interval of about 1 meter) as indicated in the data sources. The measurement accuracy of all devices is much higher compared to the error introduced by interpolation and the nudging scheme.

190 The observations used for nudging covered the region between 87.6 ° East, 139.5 ° East, 84.5° North and 87.5° North, corresponding to the MOSAiC drift from October 2019 to January 2020. During the initial phase of the drift, the DN buoys trajectories, shown in Figure 1 by colored dots, exhibited predominantly straight paths. The later part is characterized by the presence of overlapping and loops in the trajectories when the regional sea ice cover changed drift direction. These interlacement of the trajectories of different measurement platforms increase the area of the data coverage compared to the straight
195 drift, while, at the same time, introducing ambivalence in the spatio-temporal interpretation of the data. Measured parameters could be different between data measured at the same position at different times, leading to the aliasing of the observed signal.

To validate the model results, we used independent temperature and salinity data from a turbulence microstructure profiler (MSS; Schulz et al., 2022). These data were not used by the model for nudging. MSS profiles were obtained at Ocean City, on a near-daily resolution, in sets of at least 3 profiles. The profiles are averaged to 1 m vertical resolution and corrected against

200 CTD profiles, calibrated with water samples. For comparison to the model fields, we used 305 profiles (see black crosses in Figure 1).

2.5 Nudging

Nudging of the data was carried out assuming a quasi-steady-state, so that all observational data nudged the model field at the same model time. The model does not consider the time the observations were taken, which is a reasonable approximation

205 at high drift speed relative to the water velocity. At the same time, we assume no significant relation of the submesoscale baroclinic structure at different ends of the model domain. Thus, nudging the model to non-time-separated observations, we get a quasi-stationary solution that can be interpreted as the result of a dynamically justified interpolation

We applied a simple nudging algorithm: This method adds a nudging term to the evolution equation proportional to the difference between the model temperature and salinity, and the observational data at a given location. The full formulation of

210 the model is given in Androsov et al. (2019). Here we present only the tracer equations in which changes have been made and where the last term represents nudging,

$$\frac{\partial \Theta_j}{\partial t} + \frac{\partial}{\partial x_i}(\mathbf{u}_i \Theta_j) + \frac{\partial}{\partial z}(w\Theta_j) = \frac{\partial}{\partial z}\vartheta_\Theta \frac{\partial \Theta_j}{\partial z} + \nabla_2 (K_\Theta \nabla_2) \Theta_j + C_k (\Theta_{oj} - \Theta_j) \tag{3}$$

Here $i = 1, 2$, $x_1 = x$, $x_2 = y$, $u_1 = u$, and $u_2 = v$, and summation is implied over the repeating indices i; $j = 1, 2$ with $\Theta_1 = T$ and $\Theta_2 = S$ represents the potential temperature and salinity, respectively. ∇_2 is two-dimensional gradient operator.

215 ϑ_Θ and K_Θ are the corresponding vertical and horizontal diffusion coefficients. Θ_{oj} is the observational data interpolated on mesh (see below). C_k is the spatiotemporal relaxation coefficient different for different sources of observed data, $k = 1, 2$ represents the point sources (SIT) and profiles (ITP, PS-CTD and OC-CTD). The term responsible for nudging was included only for grid nodes in the immediate vicinity of observations. To do this, a mask of nodes has been precalculated for each type of observation and is explained below.

220 The observed data were separated into two groups divided by the nature of these data: The first group of data was obtained using the SIT buoys. Data from these buoys have a high temporal resolution of up to 2 minutes, and a horizontal spatial resolution up to 80 meters, both high compared to the temporal and spatial resolution of ITP profiles. At the same time, each buoy provided data from a maximum of 5 different depths. The second group of data comprises profiles obtained from ITP and PS/OS STD instruments.

225 Θ_{o1} was precalculated, and the data from the SIT buoys were interpolated onto the computational grid. Interpolation was made for two-dimensional fields for the corresponding depths of SIT buoy sensors 10,20,50,75, and 100 meters. We used a modified inverse distance weighting method (Shepard, 1968) combined with fast spatial search structure kd-tree (Maneewongvatana and Mount, 1999). Interpolation was done within a maximum distance of 1 km from each observation position and a maximum number of 30 grid nodes affected by particular measurements (Figure 2 a). The rest of the mesh nodes were masked

230 as nodes that do not participate in nudging. These up to 4 model nodes are affected by one particular observation for the model mesh with 1 km resolution. At the same time, one particular measurement affects the surrounding model mesh nodes up to

750 meters away for the mesh with 250 meters resolution, due to a limit of maximum of 30 nodes. When multiple data values were present, such as when the buoy trajectories intersected, a weighted average was calculated for a particular grid point (see Figure 2 b)). The interpolated 2-D fields were then used by the model for nudging. The model nudges the simulated fields to

235 the observation fields for each of the five depths with a spread of 3 meters from the observation depths (see Figure 2 c)). Thus, the spatiotemporal relaxation coefficient for SIT buoys takes the form:

$$C_1 = \begin{cases} T_{relax}/(1 + 0.25 \cdot |Z_{obs} - Z|^2) & : |Z - Z_{obs}| \leqslant 3 \\ 0 & : |Z - Z_{obs}| > 3 \end{cases} \tag{4}$$

where T_{relax} is the temporal relaxation coefficient equal to $1.1574 \cdot 10^{-5}$ 1/s (one day), Z is a depth of the sigma layer, Z_{obs} is one of five depths of the CTDs at the SIT buoys.

240 As a sensitivity study, a larger number of possible maximum values of neighboring nodes was also used. However, this does not significantly affect the final result. The total number of measurements was about 630000 for each parameter of salinity and temperature. The observational data obtained from the ITP profilers and ship-based and ocean-city CTDs were used in a similar manner.

In contrast to the SIT buoys, the model was nudged to the profiles by the PS- and OC-CTD only at the three nodes closest

245 to the observation position (see Figure 2 d)). If more than one profile belonged to one node, then, as in the case of SIT buoys, the inverse distance weighting method was used to average the profiles. The remaining nodes of the computational grid did not participate in nudging. Vertically the model was nudged only at the horizons where the data from the profiles were present. Linear interpolation coefficients $a(z)$ and $b(z)$ were precalculated for each cell between the standard depths where observed profiles have data. The model only reads the interpolation coefficients and reconstructs the measured values at each model

250 depth. This approach adds flexibility in setting the vertical arrangement of model sigma layers and avoids data interpolation in the process of model calculations. In this way, the spatiotemporal relaxation coefficient for profiles was $C_2 = T_{relax}$ and $\Theta_{o2} = a(z)z + b(z)$.

The significant difference in the radius of influence of the data arises from the horizontal resolution of the measurement data from the first and second groups (see prior definition). The increased radius for the SIT buoys is necessary for smoothing the

255 fields in case of crossing the trajectories of the buoys. In the case of a small radius, this leads to artificial fronts. In the case of profiles, the probability of finding measurements at different times in one place is extremely small due to the small time resolution of these instruments.

2.6 Experiment description

The deep PS-CTD profile (PS122/1_10-44) conducted from *Polarstern* during November, from the surface down to the seafloor,

260 was used as an initial condition for the whole model domain (see Figure 1 bold lines). To avoid instability in the initial conditions, the measured temperature and salinity of the surface layer were changed to constant values corresponding to a depth of 30 meters. To reduce computing time, the first run was performed on the coarse mesh described in Section 2 2.3 (see Figure 3). The resulting three-dimensional temperature and salinity fields were used as initial conditions for the simulation
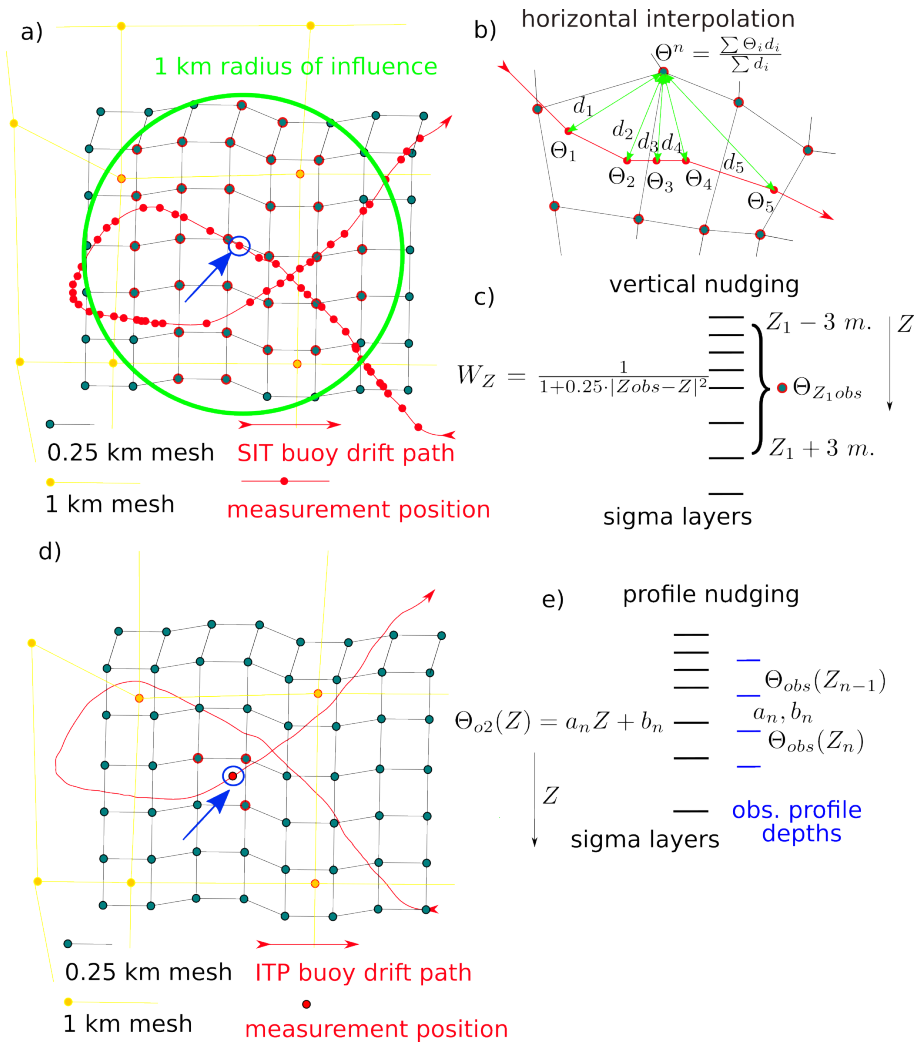
Figure 2. a), b) and c) - Schematic of interpolation and masking on the mesh. Blue and yellow circles are vertices of 0.25 and 1 km resolution meshes. The red line and circles are SIT buoy paths and measurement positions. c) - vertical relaxation weights distribution. e) - vertical interpolation of observed profile. a_n and b_n linear interpolation coefficients. Meshes vertices marked in red are influenced by the measurement marked with a blue circle.

with higher resolution. The simulation with high resolution and nudging lasted for 4 months of model time until a convergence

265   of the numerical solution was reached. In such a way temperature and salinity differences between two successive time steps do not change significantly.

    Our nudging method lead to a violation of the continuity principle and resulted in a disturbance of the velocity fields. To resolve this issue and satisfy continuity, an additional experiment was performed: A simulation with the high-resolution mesh and without nudging was run using as initial conditions the dynamical and tracer fields derived from the simulation with
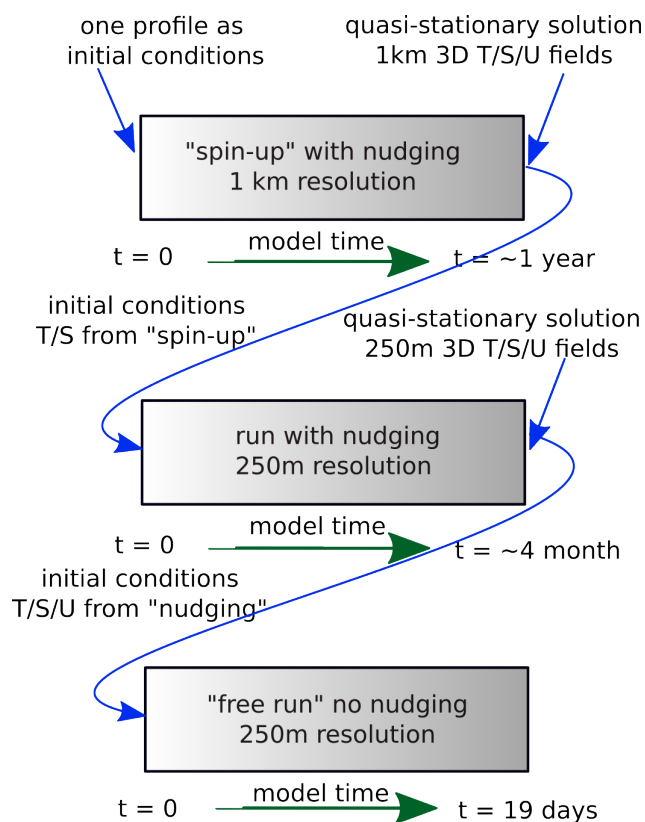
Figure 3. Schematic of conducted simulations. T/S/U are abbreviations for temperature, salinity, and velocity. The rectangles represent individual simulations.

270 nudging, hereafter termed the "free run". Results of the free run are used to analyze the dynamical field that is based on the nudged run and shows a similar structure as that run constrained by the observational data while reducing the disturbance and violation of continuity, as described above.

3 Results

3.1 Model validation

275 The MSS data set described earlier was not used for the nudging and serves here to validate the model with independent observations. Overall, the model is able to reproduce the lateral and vertical structure of the salinity field, as represented by the independent MSS observations (Figure 4 and 5a)). Snapshots of the simulation with nudging and the free run after 2.5 days (Figure 4 b, c) show similar lateral salinity gradients in the ML. After 19 days in the free run (Figure 4 d)) the lateral salinity gradient is smaller due to vertical and horizontal mixing. Salinity and temperature variability is slightly lower in the model

280 compared to the observations (Figure 5c)). The maximum deviation of the model from the observations is at the depths of
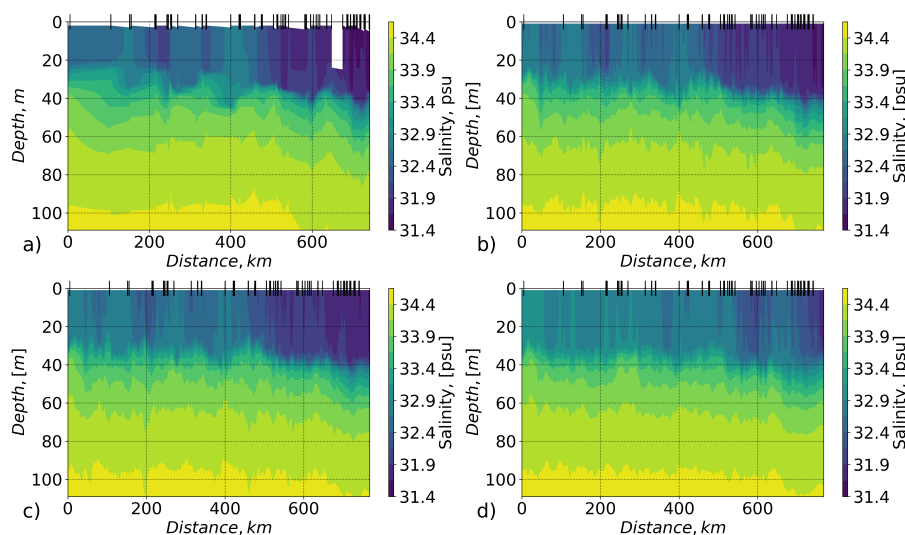
Figure 4. Salinity in the upper 120 meters along the ship drift path. The x-axis shows the distance of the ship drift with 0 km at the position of the first MSS profile. Positions of the MSS profiles are marked by black vertical lines at the top axes. a) - salinity measured by the MSS profiler Schulz et al. (2022) at Ocean City in vicinity of the ship. Here linear interpolation between MSS casts has been applied. b),c) and d) - modeled salinity at the ship positions: a) - simulation with nudging. b) - free run, 2.5 days after nudging was stopped. c) free run, 19 days after nudging was stopped.

the maximum vertical gradients in salinity (at about 37 meters) and in temperature (at about 150 meters depth). Variability of salinity decreases with time in the free run, as long as nudging takes on the role of external forcing. In the absence of nudging the model tends to dissolve eddies and slump fronts resulting in the smoothing of lateral gradients.

The statistics of the comparison between model and SIT buoy data (Table 1) show that the model deviates from the ob-
285 servations despite nudging with observational data. The largest deviation is at the positions where buoy trajectories intercept each other. These model points represent at least two different observations of the same variable at the same location. The model tends to reproduce the mean value of these overlapping observations. Moreover, the horizontal resolution of the SIT buoy observations is often higher than the spacing of the model grid, which results in larger differences between individual observed values and model output, as one model grid point covers several observations in space. The root mean square errors
290 (RMSe) are in the range of the standard deviation (SD) of the model and the observations in the surface ML (Table 1). RMSe significantly decreases for salinity underneath the halocline and about half of the SD in observation. At the same time, RMSe and SD increase for temperature underneath the halocline where temperature gradients increase (not shown).

3.2 T/S reconstruction

Cross sections along 115 °N and 86.2 °E in the modeled fields (Figure 6) indicate a decrease in ML salinity and density towards
295 the north of similar order as the smaller-scale spatial variability. The ML depth varies from about 36 in the south to 40 in the

a)

b)

c)
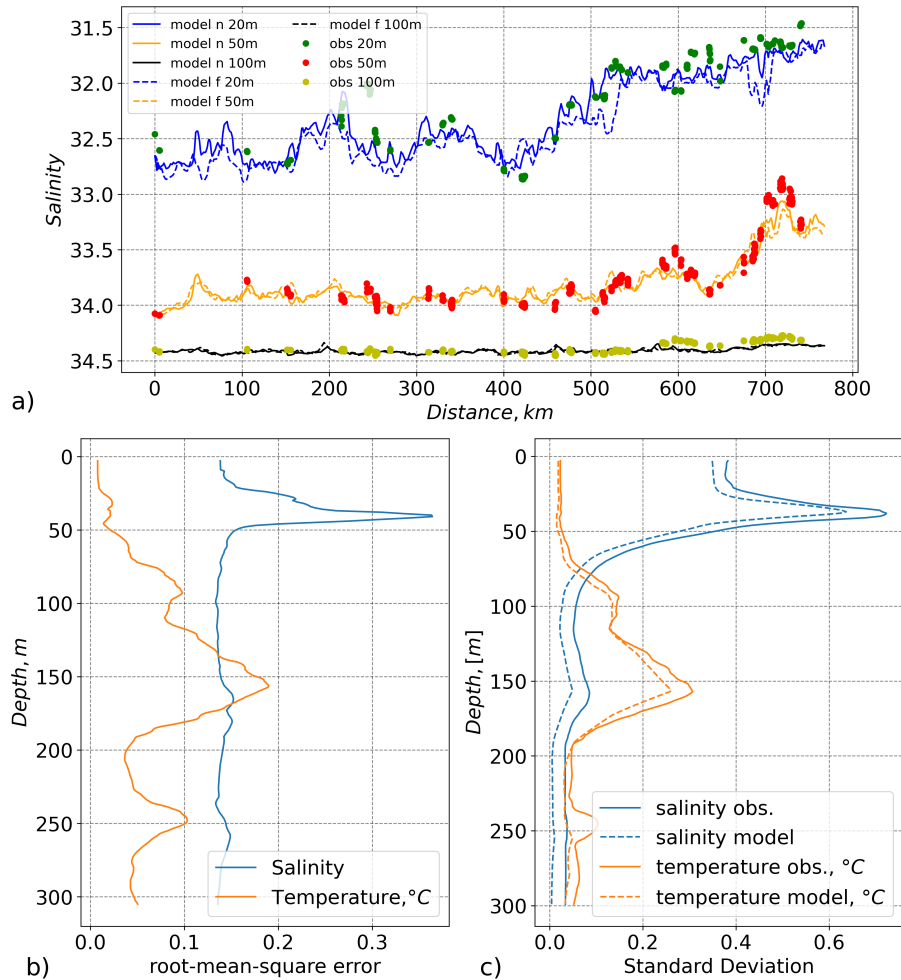
Figure 5. a) - salinity at the three depths 20,50 and 100 meters. Y-axis is inverted. Coloured dots - observed salinity data (MSS) from 10 (green), 50 (red), and 100 (orange) meters depth. Coloured lines – modeled salinity extracted at ship positions. Solid lines - model with nudging, dashed lines - free run after 2.5 days. b) - Standard deviation, blue line - observations, orange - model with nudging. c) - root mean square error of model data in comparison to observational data (MSS).

north with a minimum of 32 meters, resulting in a gradient of 0.014 m/km with 0.6 m/km standard deviation. The density in the ML, likewise, changed for about 1.1 kg/m^3 with same order variability at the model grid scale. Underneath the halocline, isopycnal lines slope by more than 10 m along the section with less smaller-scale variability than at the bottom of the ML. In the west-east direction the ML depth increases amid less small-scale variability than seen in the north-south section. Both sections show the upward slope of ML depth from the northwest to the southeast, although the west-east isopycnal slope is less uniform deeper than about 40 m than the north-south section. The same standard deviation in ML depth characterizes both directions. ML depth changes from 27 to 40 meters from east to west with a mean gradient of -0.084 m/km and 0.6 m/km gradient standard

300

Table 1. Root mean square error (RMSe) between measured by SIT buoys and modeled salinity/temperature and standard deviation (SD) of both at different depths.

depth	RMSe nudging	SD nudging	RMSe free run	SD free run	SD SIT
10	0.29 / 0.01	0.34 / 0.02	0.37 / 0.02	0.35 / 0.02	0.4 / 0.02
20	0.37 / 0.02	0.34 / 0.02	0.44 / 0.02	0.35 / 0.02	0.38 / 0.02
50	0.08 / 0.02	0.2 / 0.02	0.1 / 0.02	0.19 / 0.02	0.23 / 0.03
75	0.03 / 0.07	0.06 / 0.09	0.04 / 0.09	0.06 / 0.08	0.08 / 0.12
100	0.02 / 0.1	0.03 / 0.15	0.02 / 0.13	0.02 / 0.14	0.03 / 0.19
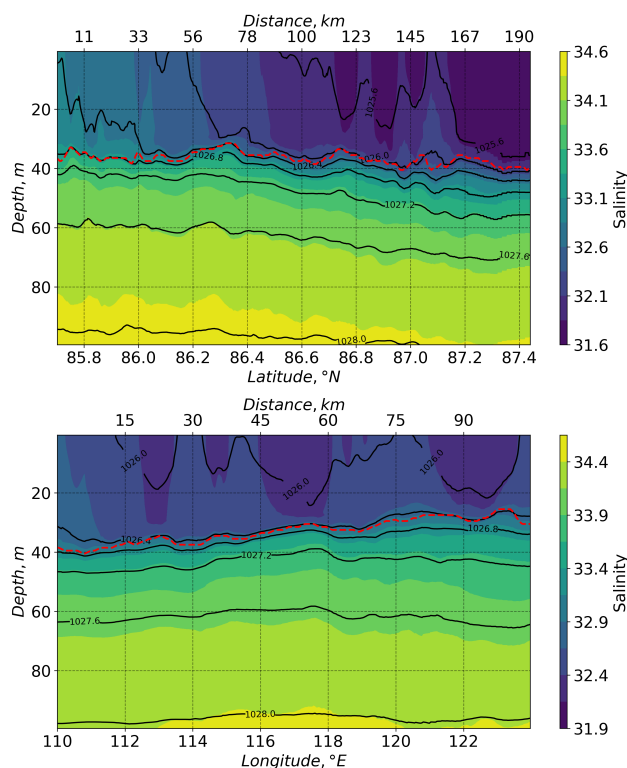
Figure 6. Cross sections along 115 °North Longitude (upper) and 86.2 °East Latitude (lower). Filled colour contours are salinity psu, and black contours are density $\mathrm{kg/m^3}$. Red dashed lines show ML depth.

deviation. Whereast the ML low-salinity (high-density) intrusions from the surface could be associated with both changes in surface heat and salt fluxes, the halocline upward buldge in the west-east section is likely associated with mesoscale features.
305 The submesoscale variability of the ML depth is most likely governed by the eddy dynamics that characterize the simulated systems as isotropic.

4 Discussion

4.1 Eddy kinetic energy

Commonly, modeled eddy kinetic energy (EKE) is defined as the difference between total kinetic energy and mean kinetic
310 energy (Wang et al., 2020). The current setup has no external forcing other than data nudging. In the absence of any external
forcing, the model does not produce significant mean velocity, resulting in negligible mean kinetic energy. Therefore, the total
kinetic energy is mainly defined by the anomaly in the velocity and linked to eddies. The EKE is calculated here as

$$EKE = (u^2 + v^2)/2. \tag{5}$$

The EKE is decreasing in the free run with time due to dissipating eddies, as an effect of surface friction, numerical diffusion,
315 etc. The absence of a mechanism to generate new EKE leads to a decrease in the free run. Meanwhile, eddies formed in the
run with nudging remain in the free run for more than 20 days. Figure 7 indicates enhanced modeled EKE activity within two
separate depth ranges, both of which are around maxima in N^2: one in the halocline and the other in the warm Atlantic Water.
Similar vertical distributions of EKE in the ice-covered central Arctic basins have been observed previously by Meneghello
et al. (2021) and modeled by Wang et al. (2020). Such a bimodal distribution of eddies was discussed in detail by Zhao et al.
320 (2014). However, we only have data from part of the winter, so we cannot analyze the effects of seasonal variability and the
associated ice conditions on the distribution of eddies. Throughout the entire time of the measurements used here, the ice cover
was already formed and consolidated with only a limited number of small openings (Nicolaus et al. (2022)). We can see a
difference in the distribution of EKE: in the southern part of the domain, the maximum energy was around the warm Atlantic
Water, whereas in the northern part, it was intensified in the halocline, just underneath the surface ML. The latter is associated
325 with stronger stratification due to high salinity gradients. At the same time, in the northern part of the considered domain,
there were sharp changes in the direction of the ice drift. This, in turn, also affected the salinity distribution of the near-surface
waters. Here it should be noted that the northern part is covered by data with many overlaps in the drift trajectories (orange
polygon in Figure 1 and 7). This, on the one hand, leads to the smoothing of the fields in the model compared to observations
where trajectories intersect. On the other hand, it can lead to the appearance of local fronts at submesoscales during nudging.
330 Using a free run partially removes the latter problem.

4.2 Eddy examples

The current velocity structure remains similar during 19 days of the free run (see Figure 8). Most of the eddies changing shape
and intensity remain close to where they formed. The number of eddies formed in the model during the fairly fast and straight
drift is similar to that in the area with overlapping drift trajectories. Most eddies travel much slower than the drift of the ship in
335 the area where the peak in EKE can be seen in the warm Atlantic Water.

The eddy dynamics differ between the northern and southern parts of our region of interest: A few of the small-scale eddies
and filaments formed at the depth of the halocline dissipate within a few days in the free run. Among the remaining, there are
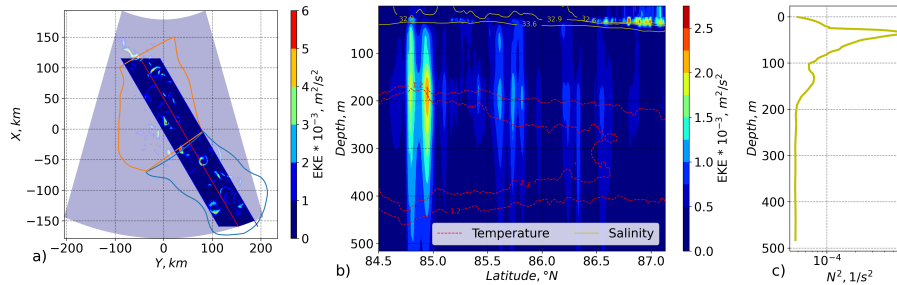
Figure 7. Modeled eddy kinetic energy and N^2 after 5 days of free run. a) - EKE at 47 meters depth. Highlighted area indicating averaging area in the stereographic projection. Area of averaging is chosen in such a way that the length of the line along the X direction is the same for any Y position. Averaging was done along X direction and covered 80 km with the center indicated by the red line. The red line was chosen in such a way that it is the longest straight line within the area covered by data. Green and orange polygons indicate the same areas as in Figure 1. b) - vertical distribution of the averaged along X direction EKE. Red dashed lines are isotherms for 1.2 and 1.3 °C. Yellow solid lines are isohalines for 33.6 and 32.9 psu. c) panel shows mean stratification computed over the area shown in panel a).
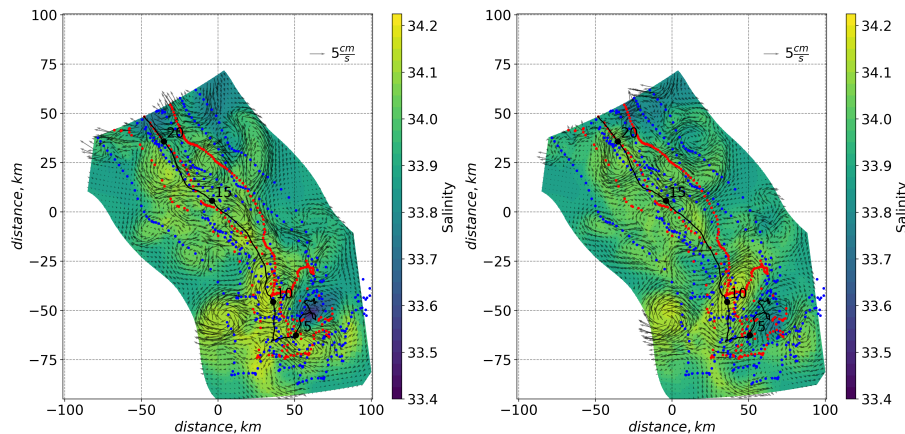
Figure 8. Salinity at 47 meters depth in the free run after 5 (left) and 19 (right) days model time, with velocity vectors (arrow top right indicate 5 cm/s) zoomed to the area with mainly straight drift (indicated by a green contour in Figure 1). The black line indicates the drift track of *Polarstern*. The black dots are the daily positions of the ship.

those that actively travel and interact with each other. Here we show an example of such eddy dynamics. Figure 9 shows that the simulated anticyclonic eddy with negative relative vorticity travels during the free run and interacts with a bigger size cyclonic
340 eddy (positive relative vorticity). The anticyclonic eddy is situated between 30 and 90 meters deep and about 5 kilometers in diameter. The cyclonic eddy is slightly larger and changes its horizontal dimensions from 7 to 10 km. The anticyclonic eddy has clearly defined contours, in contrast to the cyclonic one with more diffuse boundaries. The maximum velocities within the eddies reach 12 cm/s. The anticyclonic eddy first travels in the direction of the cyclonic eddy, then circumvents it. The cyclonic eddy remains in position before the anticyclonic eddy approaches it, but once they meet the cyclonic eddy begins to stretch
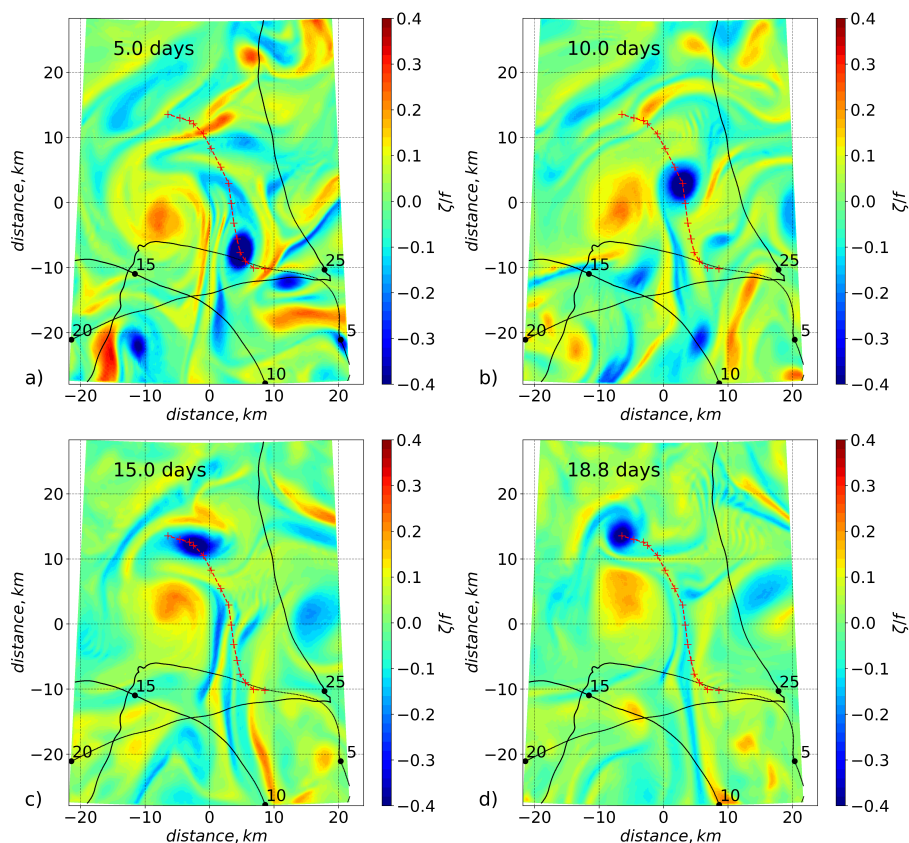
Figure 9. Snapshots of relative vorticity at the 47-meter depth in the free run. The depth of the ML depth is about 27 m. a),b),d), and c) - snapshots after 5,10,15, and 18.8 days of model time, respectively. The black line indicates the drift track of *Polarstern*. The black dots are the daily positions of the ship starting 2019-11-12. The red dashed line shows the trajectory of the center of the anticyclonic eddy described in the text, where the center was identified by eye. The position of the region shown in this figure is denoted by the cyan box in Figure 1.

345 towards the anticyclonic one. Changing shape the cyclonic eddy starts to move north as a result of the two eddies interacting. The center of the cyclonic eddy moved a total of about 7 km over 19 days. The anticyclonic eddy starts to spin around the cyclonic one and increased in translation speed. On its way, it changes shape from almost a circle to an elongated ellipse and back several times depending on its relative position to the anticyclone eddy.

This realistic example demonstrates the particular complication in the interpretation of observational data and shows that
350 the cyclonic eddy could be measured by the drifting buoys even when the drift trajectories looped and crossed each other, as the eddy position and characteristics remain the same compared to the drift. The development of the fast-traveling anticyclonic eddy could not be measured entirely by the DN as the speed of the eddy was not aligned with the buoys drift. At the same time, the distances between the buoys are larger than the eddy core diameters, which would lead to a misinterpretation during

analyzing such data by common interpolation methods. This generally applies to the DN measurements, as we only obtained a snapshot in space and time with the DN observations that were obtained over the scales set by the different DN sites.

The features of the dynamical field structure of the northern and southern parts are different. This can be explained by the nature of the ice drift. Mahadevan et al. (2010) have shown that submesoscale near-surface eddies are dissipating faster under constant unidirectional drift, something that could have happened in the southern part. At the same time, the ice drift has practically no effect on eddies without a dynamic connection to the surface, e.g. within the halocline or the warm Atlantic Water. The ice drift constantly changed direction in the northern part, and at the same time, horizontal density gradients were observed in the surface layer. Near-surface vortices are more likely to form in such conditions.

4.3 Method limitation

Several storm events were observed during the measurements, including one strong storm (Fang et al. (2023 (submitted))). Strong storms change (alter) the surface layer's dynamic nature and lead to ventilation of the upper mixed layer. In the presented quasi-stationary approach, the influence of storms is considered only indirectly through changes in temperature and salinity. Therefore, the simulation results cannot reflect the dynamics during a storm. Additionally, this approach does not account for the opening of leads, which significantly affects local heat and salt fluxes. However, through data nudging, the model indirectly considers these changes but in a smoother manner.

Furthermore, changes in the flows due to atmospheric influences are exclusively accounted for through nudging, which is determined by the density of the data and shows a smoothed pattern. In the quasi-stationary case, considering that the used observational data have a temporal spread of several months, this can result in the appearance of horizontal gradients in temperature and salinity fields. For example, we can expect a decrease in temperature and an increase in salinity in the mixed layer due to ice formation in the temporal range from November to January. Considering that the buoy drift was northwest during this time, with such a quasi-stationary approach, we can expect an increase in salinity and density in the displaced layer in the north and west directions. However, according to the simulation results, we observe the opposite pattern. There is no gradient in the west-east direction and a reverse gradient in the north (see TS reconstruction). Thus, it can be assumed that the instantaneous gradient (a gradient that could be measured at a single point in time) in the northern direction is more significant than in the reconstruction.

Despite significantly reducing the influence of regional boundaries on the final solution through increased model resolution, there remains an "internal boundary" in the model between regions with available data and regions without observations. This creates an artificial front between these two areas, determined by the initial conditions. Instabilities can occur along the boundary of this front due to the dynamics in the data-rich area and the absence of dynamics in the data-sparse area. This issue is partially mitigated by conducting a long spin-up calculation on a coarse grid, which significantly smooths the front between the areas. For future similar work, a possible solution could involve a substantial increase in the data's influence radius during the initial stage of the simulations.

In our simulations, there are also no barotropic currents or currents caused by baroclinic gradients on the scales of the Arctic basins. Typical average velocities for such currents can be 2-5 cm/s (Rabe et al., 2022, Figure 11) Rudels (2009).

However, measurements directly from the MOSAiC experiment show average velocity values of about 1 cm/s at depths of
60-200 meters (Baumann et al. (2021)). The average velocity values across the entire area in our simulations range from 1-
390   2 cm/s depending on the depth, with peaks up to 15 cm/s in eddies. Thus, we can assume that the influence of basin-scale
dynamics not considered in our work has a relatively minor affect on the final solution. In future work, it would be worthwhile
to use ocean and atmosphere reanalysis data (which utilize MOSAiC data) to provide initial and boundary conditions, if and
when they become available. Despite the coarse vertical and horizontal resolutions of these reanalyses, their usage will allow
transitioning from a quasi-stationary case to a time-dependent solution.

4.4   Summary

The MOSAiC project has collected a rich data set of physical oceanography observations in the central Arctic. Various mea-
surement techniques and tools make combining and analyzing the obtained data challenging. This paper presents ocean model
reanalyses of the first part of the MOSAiC field campaign during winter. Three-dimensional temperature and salinity fields
were reconstructed by nudging the observed data. The model setup covers the Arctic region bounded by 84.5°to 87.5°North
400   and 87.6°to 139.5°East or October 2019 to January 2020 MOSAiC drift. Using the regional FESOM-C model allowed us to
analyze the dynamic fields.

The model was further developed to suit our needs. The turbulence closure was adapted specifically for this work by modifi-
cation of the turbulence scale. Further, we extended the model with a semi-implicit method to calculate the sea level. The model
code was parallelized with MPI libraries, which made it possible to perform calculations with the required resolution and 1.3
405   million horizontal nodes. Considering 240 vertical layers for the current setup, the number of calculated model points exceeds
3.3 times the eddy-permitting global mesh with a quasi-uniform resolution of 15 km in the FESOM2 setup (Danilov et al.,
2017). Our developed setup of the FESOM-C model with an unstructured mesh makes it possible to mitigate the influence of
boundary conditions on the area of interest. Near-surface and deep submesoscale processes are resolved by the high horizontal
resolution of up to 250 m and the vertical resolution of up to 1 m. A simple algorithm was developed to nudge the model to
410   the observed data, that makes it possible to use a large amount of data from different measuring systems. More than 630,000
single-point temperatures and salinity and over a thousand vertical profiles were nudged by the model.

We validated the model output against independent data that were not used for nudging. The vertical and horizontal distribu-
tions of temperature and salinity are well reproduced by the model. We found the main discrepancies between independent and
modeled data at the intersections of the drift trajectories of the buoys. Buoys have overlapping tracks due to the ice drift loops,
415   for example, during rapid changes in the wind direction. These not-quite-synoptic measurements lead to a gridded (nudging)
field that is not necessarily equal to individual observed values as a result of the weighted mean interpolation.

By utilizing the data nudging method we have been able to reconstruct dynamically consistent three-dimensional temper-
ature, salinity, and density fields. The results of our simulation allow analyzing the horizontal and vertical distribution of
temperature, salinity, and velocity on a regular grid. Our analysis of the dynamic characteristics revealed the existence of two
420   separate depth ranges of enhanced eddy kinetic energy located around two maxima in buoyancy frequency: the halocline depth

and the depth of the warm Atlantic Water. The model resolves several stationary warm-Atlantic-Water eddies and provides insights into the associated dynamics that would not be possible by analyzing the observations alone.

Code and data availability. The FESOM-C code and model setup used in this study can be found under DOI:https://doi.org/10.5281/zenodo.8004904. Modelling results for 6 vertical layers and 5 temporal layers of the free run created during this study is openly available in the Zenodo open
425   data repository and can also be found at the provided link. Rest of the modelling data are available upon request by contacting the corresponding authors.

Author contributions. IK, BR, YCF and AA were responsible for the initial conceptualization of the study. IK developed the data nudging method, model setup, simulations, processing the results and wrote the paper with a strong contribution from BR and AA. Providing, post processing and the curation the observational data, deploying the instruments in the field: BR, YCF, MH, IK, AQZ, ST, KS, VM, IF, MJ. AA,
430   IK, SH, VF developing the FESOM-C code. All co-authors reviewed the manuscript and contributed to the writing and final editing.

Competing interests. Ilker Fer is a member of the editorial board of Ocean Science.

Acknowledgements. Data presented in this paper were produced as part of the international Multidisciplinary drifting Observatory for the Study of the Arctic Climate (MOSAiC) with the tag MOSAiC20192020 (grant numbers AWI_PS122_00 and AFMOSAiC-1_00). The instruments were funded as part of the MIDO (Multidisciplinary Ice-based Drifting Observatory) infrastructure. The study contributes to
435   the Changing Arctic Ocean (CAO) program, jointly funded by the UKRI Natural Environment Research Council (NERC) and the BMBF, project Advective Pathways of nutrients and key Ecological substances in the ARctic (APEAR) grants NE/R012865/1, NE/R012865/2 and #03V01461; the project EPICA in the research theme MARE:N - Polarforschung/MOSAiC funded by the German Federal Ministry for Education and Research with funding number 03F0889A; the European Commission for EU H2020 grant no. 101003472 (project Arctic PASSION), and the AROMA (Arctic Ocean mixing processes and vertical fluxes of energy and matter) project by the Research Council of
440   Norway, grant number 294396. We thank the administrators of the AWI cluster Ollie and Albedo, where the simulations took place, for their continual support and patience. Full acknowledgments are available in Nixdorf et al. (2021).

References

Androsov, A., Rubino, A., Romeiser, R., and Sein, D. V.: Open-ocean convection in the Greenland Sea: preconditioning through a mesoscale chimney and detectability in SAR imagery studied with a hierarchy of nested numerical models, Meteorologische Zeitschrift, 14, 693–702, https://doi.org/10.1127/0941-2948/2005/0078, 2005.

Androsov, A., Nerger, L., Schnur, R., Schröter, J., Albertella, A., Rummel, R., Savcenko, R., Bosch, W., Skachko, S., and Danilov, S.: On the assimilation of absolute geodetic dynamic topography in a global ocean model: impact on the deep ocean state, Journal of Geodesy, 93, 141–157, https://doi.org/10.1007/s00190-018-1151-1, 2018.

Androsov, A., Fofonova, V., Kuznetsov, I., Danilov, S., Rakowsky, N., Harig, S., Brix, H., and Helen Wiltshire, K.: FESOM-C v.2: Coastal dynamics on hybrid unstructured meshes, Geoscientific Model Development, 12, 1009–1028, https://doi.org/10.5194/gmd-12-1009-2019, 2019.

Androsov, A., Boebel, O., Schröter, J., Danilov, S., Macrander, A., and Ivanciu, I.: Ocean Bottom Pressure Variability: Can It Be Reliably Modeled?, Journal of Geophysical Research: Oceans, 125, https://doi.org/10.1029/2019JC015469, 2020.

Baumann, T., Fer, I., Bryhni, H., Peterson, A. K., Allerholt, J., Fang, Y.-C., Hoppmann, M., Karam, S., Koenig, Z., Kong, B., Mohrholz, V., Muilwijk, M., Schaffer, J., Schulz, K., Sukhikh, N., and Tippenhauer, S.: Under-ice current measurements during MOSAiC from a 75 kHz acoustic Doppler profiler, https://doi.org/10.1594/PANGAEA.934792, 2021.

Courtier, P., Thépaut, J.-N., and Hollingsworth, A.: A strategy for operational implementation of 4D-Var, using an incremental approach, Quarterly Journal of the Royal Meteorological Society, 120, 1367–1387, https://doi.org/10.1002/qj.49712051912, 1994.

Danilov, S. and Androsov, A.: Cell-vertex discretization of shallow water equations on mixed unstructured meshes, Ocean Dynamics, 65, 33–47, https://doi.org/10.1007/s10236-014-0790-x, 2015.

Danilov, S., Sidorenko, D., Wang, Q., and Jung, T.: The Finite-volumE Sea ice–Ocean Model (FESOM2), Geoscientific Model Development, 10, 765–789, https://doi.org/10.5194/gmd-10-765-2017, 2017.

Dmitrenko, I. A., Kirillov, S. A., Ivanov, V. V., and Woodgate, R. A.: Mesoscale Atlantic water eddy off the Laptev Sea continental slope carries the signature of upstream interaction, Journal of Geophysical Research: Oceans, 113, https://doi.org/10.1029/2007JC004491, 2008.

Fang, Y.-C., Rabe, B., Kuznetsov, I., Hoppmann, M., Tippenhauer, S., Regnery, J., He, H., and Li, T.: Early winter upper-ocean variability in the Amundsen Basin of the Arctic Ocean from the MOSAiC expedition, Earth System Science Data, 2023 (submitted).

Fofonova, V., Androsov, A., Sander, L., Kuznetsov, I., Amorim, F., Hass, H. C., and Wiltshire, K. H.: Non-linear aspects of the tidal dynamics in the Sylt-Rømø Bight, south-eastern North Sea, Ocean Science, 15, 1761–1782, https://doi.org/10.5194/os-15-1761-2019, 2019.

Gula, J., Taylor, J., Shcherbina, A., and Mahadevan, A.: Chapter 8 - Submesoscale processes and mixing, in: Ocean Mixing, edited by Meredith, M. and Naveira Garabato, A., pp. 181–214, Elsevier, https://doi.org/10.1016/B978-0-12-821512-8.00015-3, 2022.

Hoppmann, M., Kuznetsov, I., Fang, Y.-C., and Rabe, B.: Mesoscale observations of temperature and salinity in the Arctic Transpolar Drift: a high-resolution dataset from the MOSAiC Distributed Network, Earth System Science Data Discussions, 2022, 1–33, https://doi.org/10.5194/essd-2022-66, 2022.

Hordoir, R., Skagseth, Ø., Ingvaldsen, R. B., Sandø, A. B., Löptien, U., Dietze, H., Gierisch, A. M. U., Assmann, K. M., Lundesgaard, Ø., and Lind, S.: Changes in Arctic Stratification and Mixed Layer Depth Cycle: A Modeling Analysis, Journal of Geophysical Research: Oceans, 127, https://doi.org/10.1029/2021JC017270, 2022.

480 Krumpen, T. and Sokolov, V.: The Expedition AF122/1 : Setting up the MOSAiC Distributed Network in October 2019 with Research
     Vessel AKADEMIK FEDOROV, techreport, Berichte zur Polar- und Meeresforschung = Reports on polar and marine research, Alfred
     Wegener Institute for Polar and Marine Research, Bremerhaven, https://doi.org/10.2312/BzPM_0744_2020, 2020.

     Kuznetsov, I., Androsov, A., Fofonova, V., Danilov, S., Rakowsky, N., Harig, S., and Wiltshire, K. H.: Evaluation and Application of
     Newly Designed Finite Volume Coastal Model FESOM-C, Effect of Variable Resolution in the Southeastern North Sea, Water, 12,
485 https://doi.org/10.3390/w12051412, 2020.

     Li, J., Liao, W.-k., Choudhary, A., Ross, R., Thakur, R., Gropp, W., Latham, R., Siegel, A., Gallagher, B., and Zingale, M.: Parallel
     NetCDF: A High-Performance Scientific I/O Interface, in: Proceedings of the 2003 ACM/IEEE Conference on Supercomputing, SC
     '03, p. 39, Association for Computing Machinery, New York, NY, USA, https://doi.org/10.1145/1048935.1050189, 2003.

     Li, Z., Saad, Y., and Sosonkina, M.: pARMS: a parallel version of the algebraic recursive multilevel solver, Numerical Linear Algebra
490 with Applications, 10, 485–509, https://doi.org/10.1002/nla.325.

     Llinás, L., Pickart, R. S., Mathis, J. T., and Smith, S. L.: Zooplankton inside an Arctic Ocean cold-core eddy: Probable origin and fate,
     Deep Sea Research Part II: Topical Studies in Oceanography, 56, 1290–1304, https://doi.org/10.1016/j.dsr2.2008.10.020, the Western
     Artic Shelf-Basin Interactions (SBI)Project, Vol.2, 2009.

     Lovecchio, E., Gruber, N., Münnich, M., and Frenger, I.: On the Processes Sustaining Biological Production in the Offshore Prop-
495 agating Eddies of the Northern Canary Upwelling System, Journal of Geophysical Research: Oceans, 127, e2021JC017691,
     https://doi.org/10.1029/2021JC017691, e2021JC017691 2021JC017691, 2022.

     Lyu, G., Serra, N., Zhou, M., and Stammer, D.: Arctic sea level variability from high-resolution model simulations and implications for
     the Arctic observing system, Ocean Science, 18, 51–66, https://doi.org/10.5194/os-18-51-2022, 2022.

     Mahadevan, A.: The Impact of Submesoscale Physics on Primary Productivity of Plankton, Annual Review of Marine Science, 8, 161–184,
500 https://doi.org/10.1146/annurev-marine-010814-015912, 2016.

     Mahadevan, A., Tandon, A., and Ferrari, R.: Rapid changes in mixed layer stratification driven by submesoscale instabilities and winds,
     Journal of Geophysical Research, 115, https://doi.org/10.1029/2008JC005203, 2010.

     Maneewongvatana, S. and Mount, D.: It's okay to be skinny, if your friends are fat, Center for Geometric Computing 4th Annual Workshop
     on Computational Geometry, 1999.

505 Manucharyan, G. E. and Thompson, A. F.: Submesoscale Sea Ice-Ocean Interactions in Marginal Ice Zones, Journal of Geophysical
     Research: Oceans, 122, 9455–9475, https://doi.org/10.1002/2017JC012895, 2017.

     Marcinko, C. L. J., Martin, A. P., and Allen, J. T.: Characterizing horizontal variability and energy spectra in the scpA/scp rctic scpO/scp
     cean halocline, Journal of Geophysical Research: Oceans, 120, 436–450, https://doi.org/10.1002/2014JC010381, 2015.

     Maslowski, W., Kinney, J. C., Marble, D. C., and Jakacki, J.: Towards Eddy-Resolving Models of the Arctic Ocean, pp. 241–264, American
510 Geophysical Union (AGU), https://doi.org/10.1029/177GM16, 2008.

     Meneghello, G., Marshall, J., Lique, C., Isachsen, P. E., Doddridge, E., Campin, J.-M., Regan, H., and Talandier, C.: Genesis and Decay
     of Mesoscale Baroclinic Eddies in the Seasonally Ice-Covered Interior Arctic Ocean, Journal of Physical Oceanography, 51, 115 – 129,
     https://doi.org/10.1175/JPO-D-20-0054.1, 2021.

     Mensa, J. A. and Timmermans, M.-L.: Characterizing the seasonal cycle of upper-ocean flows under multi-year sea ice, Ocean Modelling,
515 113, 115–130, https://doi.org/10.1016/j.ocemod.2017.03.009, 2017.

     Mogensen, K., Alonso-Balmaseda, M., Weaver, A., Martin, M., and Vidard, A.: NEMOVAR: A variational data assimilation system for
     the NEMO ocean model, https://doi.org/10.21957/3yj3mh16iq, 2009.

Neder, C., Fofonova, V., Androsov, A., Kuznetsov, I., Abele, D., Falk, U., Schloss, I. R., Sahade, R., and Jerosch, K.: Modelling suspended particulate matter dynamics at an Antarctic fjord impacted by glacier melt, Journal of Marine Systems, 231, 103 734, https://doi.org/10.1016/j.jmarsys.2022.103734, 2022.

Nerger, L., Tang, Q., and Mu, L.: Efficient ensemble data assimilation for coupled models with the Parallel Data Assimilation Framework: example of AWI-CM (AWI-CM-PDAF 1.0), Geoscientific Model Development, 13, 4305–4321, https://doi.org/10.5194/gmd-13-4305-2020, 2020.

Nicolaus, M., Perovich, D. K., Spreen, G., Granskog, M. A., von Albedyll, L., Angelopoulos, M., Anhaus, P., Arndt, S., Belter, H. J., Bessonov, V., Birnbaum, G., Brauchle, J., Calmer, R., Cardellach, E., Cheng, B., Clemens-Sewall, D., Dadic, R., Damm, E., de Boer, G., Demir, O., Dethloff, K., Divine, D. V., Fong, A. A., Fons, S., Frey, M. M., Fuchs, N., Gabarró, C., Gerland, S., Goessling, H. F., Gradinger, R., Haapala, J., Haas, C., Hamilton, J., Hannula, H.-R., Hendricks, S., Herber, A., Heuzé, C., Hoppmann, M., Høyland, K. V., Huntemann, M., Hutchings, J. K., Hwang, B., Itkin, P., Jacobi, H.-W., Jaggi, M., Jutila, A., Kaleschke, L., Katlein, C., Kolabutin, N., Krampe, D., Kristensen, S. S., Krumpen, T., Kurtz, N., Lampert, A., Lange, B. A., Lei, R., Light, B., Linhardt, F., Liston, G. E., Loose, B., Macfarlane, A. R., Mahmud, M., Matero, I. O., Maus, S., Morgenstern, A., Naderpour, R., Nandan, V., Niubom, A., Oggier, M., Oppelt, N., Pätzold, F., Perron, C., Petrovsky, T., Pirazzini, R., Polashenski, C., Rabe, B., Raphael, I. A., Regnery, J., Rex, M., Ricker, R., Riemann-Campe, K., Rinke, A., Rohde, J., Salganik, E., Scharien, R. K., Schiller, M., Schneebeli, M., Semmling, M., Shimanchuk, E., Shupe, M. D., Smith, M. M., Smolyanitsky, V., Sokolov, V., Stanton, T., Stroeve, J., Thielke, L., Timofeeva, A., Tonboe, R. T., Tavri, A., Tsamados, M., Wagner, D. N., Watkins, D., Webster, M., and Wendisch, M.: Overview of the MOSAiC expedition: Snow and sea ice, Elementa: Science of the Anthropocene, 10, https://doi.org/10.1525/elementa.2021.000046, 2022.

Nishino, S., Kawaguchi, Y., Fujiwara, A., Shiozaki, T., Aoyama, M., Harada, N., and Kikuchi, T.: Biogeochemical Anatomy of a Cyclonic Warm-Core Eddy in the Arctic Ocean, Geophysical Research Letters, 45, 11,284–11,292, https://doi.org/10.1029/2018GL079659, 2018.

Nixdorf, U., Dethloff, K., Rex, M., Shupe, M., Sommerfeld, A., Perovich, D. K., Nicolaus, M., Heuzé, C., Rabe, B., Loose, B., Damm, E., Gradinger, R., Fong, A., Maslowski, W., Rinke, A., Kwok, R., Spreen, G., Wendisch, M., Herber, A., Hirsekorn, M., Mohaupt, V., Frickenhaus, S., Immerz, A., Weiss-Tuider, K., König, B., Mengedoht, D., Regnery, J., Gerchow, P., Ransby, D., Krumpen, T., Morgenstern, A., Haas, C., Kanzow, T., Rack, F. R., Saitzev, V., Sokolov, V., Makarov, A., Schwarze, S., Wunderlich, T., Wurr, K., and Boetius, A.: MOSAiC Extended Acknowledgement, https://doi.org/10.5281/zenodo.5541624, 2021.

Nurser, A. J. G. and Bacon, S.: The Rossby radius in the Arctic Ocean, Ocean Science, 10, 967–975, https://doi.org/10.5194/os-10-967-2014, 2014.

Omand, M. M., D'Asaro, E. A., Lee, C. M., Perry, M. J., Briggs, N., Cetinić, I., and Mahadevan, A.: Eddy-driven subduction exports particulate organic carbon from the spring bloom, Science, 348, 222–225, https://doi.org/10.1126/science.1260062, 2015.

Oziel, L., Schourup-Kristensen, V., Wekerle, C., and Hauck, J.: The Pan-Arctic Continental Slope as an Intensifying Conveyer Belt for Nutrients in the Central Arctic Ocean (1985–2015), Global Biogeochemical Cycles, 36, e2021GB007 268, https://doi.org/10.1029/2021GB007268, 2022.

O'Brien, M. C., Melling, H., Pedersen, T. F., and Macdonald, R. W.: The role of eddies on particle flux in the Canada Basin of the Arctic Ocean, Deep Sea Research Part I: Oceanographic Research Papers, 71, 1–20, https://doi.org/10.1016/j.dsr.2012.10.004, 2013.

Pnyushkov, A., Polyakov, I. V., Padman, L., and Nguyen, A. T.: Structure and dynamics of mesoscale eddies over the Laptev Sea continental slope in the Arctic Ocean, Ocean Science, 14, 1329–1347, https://doi.org/10.5194/os-14-1329-2018, 2018.

555   Quintanilla-Zurita, A. and et al.: Intrahalocline eddy in the central Arctic from distributed observations during the MOSAiC winter, Ocean Science, (in prep.).

Rabe, B., Heuzé, C., Regnery, J., Aksenov, Y., Allerholt, J., Athanase, M., Bai, Y., Basque, C., Bauch, D., Baumann, T. M., Chen, D., Cole, S. T., Craw, L., Davies, A., Damm, E., Dethloff, K., Divine, D. V., Doglioni, F., Ebert, F., Fang, Y.-C., Fer, I., Fong, A. A., Gradinger, R., Granskog, M. A., Graupner, R., Haas, C., He, H., He, Y., Hoppmann, M., Janout, M., Kadko, D., Kanzow, T., Karam,
560   S., Kawaguchi, Y., Koenig, Z., Kong, B., Krishfield, R. A., Krumpen, T., Kuhlmey, D., Kuznetsov, I., Lan, M., Laukert, G., Lei, R., Li, T., Torres-Valdés, S., Lin, L., Lin, L., Liu, H., Liu, N., Loose, B., Ma, X., McKay, R., Mallet, M., Mallett, R. D. C., Maslowski, W., Mertens, C., Mohrholz, V., Muilwijk, M., Nicolaus, M., O'Brien, J. K., Perovich, D., Ren, J., Rex, M., Ribeiro, N., Rinke, A., Schaffer, J., Schuffenhauer, I., Schulz, K., Shupe, M. D., Shaw, W., Sokolov, V., Sommerfeld, A., Spreen, G., Stanton, T., Stephens, M., Su, J., Sukhikh, N., Sundfjord, A., Thomisch, K., Tippenhauer, S., Toole, J. M., Vredenborg, M., Walter, M., Wang, H., Wang, L., Wang, Y.,
565   Wendisch, M., Zhao, J., Zhou, M., and Zhu, J.: Overview of the MOSAiC expedition: Physical oceanography, Elementa: Science of the Anthropocene, 10, https://doi.org/10.1525/elementa.2021.00062, 2022.

Regan, H., Lique, C., Talandier, C., and Meneghello, G.: Response of Total and Eddy Kinetic Energy to the Recent Spinup of the Beaufort Gyre, Journal of Physical Oceanography, 50, 575 – 594, https://doi.org/10.1175/JPO-D-19-0234.1, 2020.

Rubino, A., Androssov, A., and Dotsenko, S.: Intrinsic dynamics and long-term evolution of a convectively generated oceanic vortex in
570   the Greenland Sea, Geophysical Research Letters, 34, https://doi.org/10.1029/2007GL030634, 2007.

Rudels, B.: Arctic Ocean Circulation, in: Encyclopedia of Ocean Sciences (Second Edition), edited by Steele, J. H., pp. 211–225, Academic Press, Oxford, second edition edn., https://doi.org/10.1016/B978-012374473-9.00601-9, 2009.

Ruggiero, G. A., Ourmières, Y., Cosme, E., Blum, J., Auroux, D., and Verron, J.: Data assimilation experiments using diffusive back-and-forth nudging for the NEMO ocean model, Nonlinear Processes in Geophysics, 22, 233–248, https://doi.org/10.5194/npg-22-233-2015,
575   2015.

Schulz, K., Mohrholz, V., Fer, I., Janout, M. A., Hoppmann, M., Schaffer, J., Koenig, Z., Rabe, B., Heuzé, C., Regnery, J., Allerholt, J., Fang, Y.-C., He, H., Kanzow, T., Karam, S., Kuznetsov, I., Kong, B., Liu, H., Muilwijk, M., Schuffenhauer, I., Sukhikh, N., Sundfjord, A., and Tippenhauer, S.: Turbulent microstructure profile (MSS) measurements from the MOSAiC drift, Arctic Ocean, https://doi.org/10.1594/PANGAEA.939816, 2022.

580   Scott, R. M., Pickart, R. S., Lin, P., Münchow, A., Li, M., Stockwell, D. A., and Brearley, J. A.: Three-Dimensional Structure of a Cold-Core Arctic Eddy Interacting with the Chukchi Slope Current, Journal of Geophysical Research: Oceans, 124, 8375–8391, https://doi.org/10.1029/2019JC015523, 2019.

Shepard, D.: A Two-Dimensional Interpolation Function for Irregularly-Spaced Data, in: Proceedings of the 1968 23rd ACM National Conference, ACM '68, p. 517–524, Association for Computing Machinery, New York, NY, USA,
585   https://doi.org/10.1145/800186.810616, 1968.

Shupe, M., Rex, M., Dethloff, K., Damm, E., Fong, A. A., Gradinger, R., Heuzé, C., Loose, B., Makarov, A. S., Maslowski, W., Nicolaus, M., Perovich, D. K., Rabe, B., Rinke, A., Sokolov, V., and Sommerfeld, A.: Arctic Report Card 2020: The MOSAiC Expedition: A Year Drifting with the Arctic Sea Ice, Arctic Report Card, https://doi.org/10.25923/9g3v-xh92, 2020.

Sokolovskiy, M. A. and Verron, J.: Dynamics of Vortex Structures in a Stratified Rotating Fluid, Dynamics of Vortex Structures in a
590   Stratified Rotating Fluid, 2013.

Tippenhauer, S., Vredenborg, M., Heuzé, C., Ulfsbo, A., Rabe, B., Allerholt, J., Balmonte, J. P., Campbell, R. G., Castellani, G., Chamberlain, E., Creamean, J., D'Angelo, A., Dietrich, U., Droste, E., Eggers, L., Fang, Y.-C., Fong, A. A., Gardner, J., Graupner, R.,

Grosse, J., He, H., Hildebrandt, N., Hoppe, C. J. M., Hoppmann, M., Kanzow, T., Karam, S., Koenig, Z., Kong, B., Kuhlmey, D.,
Kuznetsov, I., Lan, M., Liu, H., Mallet, M., Mohrholz, V., Muilwijk, M., Müller, O., Olsen, L. M., Rember, R., Ren, J., Sakinan,
595   S., Schaffer, J., Schmidt, K., Schuffenhauer, I., Schulz, K., Shoemaker, K., Spahic, S., Sukhikh, N., Svenson, A., Torres-Valdés, S.,
Torstensson, A., Wischnewski, L., and Zhuang, Y.: Physical oceanography based on ship CTD during POLARSTERN cruise PS122.,
https://doi.org/10.1594/PANGAEA.959963, 2023a.

Tippenhauer, S., Vredenborg, M., Heuzé, C., Ulfsbo, A., Rabe, B., Allerholt, J., Balmonte, J. P., Campbell, R. G., Castellani, G., Cham-
berlain, E., Creamean, J., D'Angelo, A., Dietrich, U., Droste, E., Eggers, L., Fang, Y.-C., Fong, A. A., Gardner, J., Graupner, R.,
600   Grosse, J., He, H., Hildebrandt, N., Hoppe, C. J. M., Hoppmann, M., Kanzow, T., Karam, S., Koenig, Z., Kong, B., Kuhlmey, D.,
Kuznetsov, I., Lan, M., Liu, H., Mallet, M., Mohrholz, V., Muilwijk, M., Müller, O., Olsen, L. M., Rember, R., Ren, J., Sakinan,
S., Schaffer, J., Schmidt, K., Schuffenhauer, I., Schulz, K., Shoemaker, K., Spahic, S., Sukhikh, N., Svenson, A., Torres-Valdés, S.,
Torstensson, A., Wischnewski, L., and Zhuang, Y.: Physical oceanography based on Ocean City CTD during POLARSTERN cruise
PS122., https://doi.org/10.1594/PANGAEA.959964, 2023b.

605 Toole, J. M. and Krishfield, R. A.: Oceanographic Institution Ice-Tethered Profiler Program (2016). Ice-Tethered Profiler observations:
Vertical profiles of temperature, salinity, oxygen, and ocean velocity from an Ice-Tethered Profiler buoy system. [indicate subset used].
NOAA National Centers for Environmental Information. Dataset., Tech. rep., https://doi.org/10.7289/v5mw2f7x, accessed 13.7.2021,
2016.

von Appen, W.-J., Baumann, T. M., Janout, M., Koldunov, N., Lenn, Y.-D., Pickart, R. S., Scott, R. B., and Wang, Q.: Eddies and the
610   Distribution of Eddy Kinetic Energy in the Arctic Ocean, Oceanography, 35, pp. 42–51, https://www.jstor.org/stable/27182695, 2022.

Wang, Q., Koldunov, N. V., Danilov, S., Sidorenko, D., Wekerle, C., Scholz, P., Bashmachnikov, I. L., and Jung, T.: Eddy Kinetic
Energy in the Arctic Ocean From a Global Simulation With a 1-km Arctic, Geophysical Research Letters, 47, e2020GL088 550,
https://doi.org/10.1029/2020GL088550, 2020.

Watanabe, E.: Beaufort shelf break eddies and shelf-basin exchange of Pacific summer water in the western Arctic Ocean detected by
615   satellite and modeling analyses, Journal of Geophysical Research: Oceans, 116, https://doi.org/10.1029/2010JC006259, 2011.

Zhao, M., Timmermans, M.-L., Cole, S., Krishfield, R., Proshutinsky, A., and Toole, J.: Characterizing the eddy field in the Arctic Ocean
halocline, Journal of Geophysical Research: Oceans, 119, 8800–8817, https://doi.org/10.1002/2014JC010488, 2014.

Zhao, M., Timmermans, M.-L., Cole, S., Krishfield, R., and Toole, J.: Evolution of the eddy field in the Arctic Ocean's Canada Basin,
2005-2015, Geophysical Research Letters, 43, 8106–8114, https://doi.org/10.1002/2016GL069671, 2016.